LETTERS

Tomographic imaging using the nonlinear response of magnetic particles

Bernhard Gleich[1]* & Jürgen Weizenecker[1]*

The use of contrast agents and tracers in medical imaging has a long history[1–7]. They provide important information for diagnosis and therapy, but for some desired applications, a higher resolution is required than can be obtained using the currently available medical imaging techniques. Consider, for example, the use of magnetic tracers in magnetic resonance imaging: detection thresholds for *in vitro*[8] and *in vivo*[9] imaging are such that the background signal from the host tissue is a crucial limiting factor. A sensitive method for detecting the magnetic particles directly is to measure their magnetic fields using relaxometry[10]; but this approach has the drawback that the inverse problem (associated with transforming the data into a spatial image) is ill posed and therefore yields low spatial resolution. Here we present a method for obtaining a high-resolution image of such tracers that takes advantage of the nonlinear magnetization curve of small magnetic particles. Initial 'phantom' experiments are reported that demonstrate the feasibility of the imaging method. The resolution that we achieve is already well below 1 mm. We evaluate the prospects for further improvement, and show that the method has the potential to be developed into an imaging method characterized by both high spatial resolution as well as high sensitivity.

We first introduce the general concept of magnetic particle imaging (MPI). MPI relies on the nonlinearity of the magnetization curves of ferromagnetic material and the fact that the particle magnetization saturates at some magnetic field strength. If an oscillating magnetic field, called the 'modulation field', is applied, with frequency f_1 and sufficiently high amplitude A, the magnetic material will exhibit a magnetization $M(t)$, where t is time. $M(t)$ contains not only the drive frequency f_1, but also a series of harmonic frequencies (Fig. 1a). These higher frequencies can be easily separated from the received signal by means of appropriate filtering.

If the magnetic particles are also exposed to a time constant magnetic field with a sufficiently large magnitude, they saturate and the generation of harmonics is suppressed (Fig. 1b). Selective suppression of the harmonics is employed for the spatial encoding as follows. In addition to the modulation field, a time-independent field is superimposed (field plot in Fig. 2a) that vanishes in the centre of the imaging device (the field-free point, FFP) and increases in magnitude towards the edges. This field is called the 'selection field'. If there is any magnetic material at the position of the FFP it will produce a signal containing higher harmonics. But only the magnetic material located at the FFP will respond to the a.c. modulation field. All other magnetic material remains in the state of saturation. By steering the FFP through the volume of interest, a tomographic image can be generated. (As a spatial variation in one direction of one field component is in general accompanied by a spatial variation of another component in another direction, only a single selection field is needed in MPI to obtain a three-dimensional spatial encoding.) The movement can be performed by moving the whole coil assembly or by moving the object within the coil assembly. For simplicity, we assumed a low amplitude of the modulation field. Otherwise, the a.c. field shifts the FFP significantly.

In summary, to form an image, magnetic tracer material has to be applied to, or introduced into, the object. The object is placed in the selection field, and a weak magnetic modulation field is superimposed. Finally the object is moved (spatial encoding) to discrete positions and the magnitudes of the harmonics are recorded. An image of the magnetic tracer in the object is directly obtained by mapping the magnitude of the harmonics.

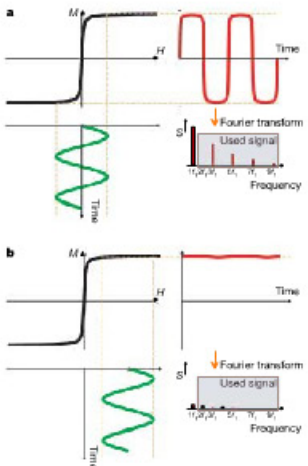

Figure 1 | Response of magnetic particles to an external magnetic field. **a**, An oscillating magnetic field (H, modulation field, green curve) is applied to the magnetic material at a single frequency f_1. As the magnetization curve (M, black curve) is nonlinear, the resulting time-dependent magnetization (red curve) exhibits higher harmonics, as is shown in the Fourier-transformed signal (S, red bars). **b**, A time-independent field is added to the modulation field. The oscillating field does not significantly change the magnetization of the material, as it is always in saturation. In this state, harmonics of the oscillating field are almost non-existent. The grey box indicates those harmonics used for image formation. The signal at f_1 is not used, as it is small compared to the superimposed induced modulation field signal, and therefore difficult to isolate.

[1]Philips Research Hamburg, Röntgenstrasse 24-26, D-22335 Hamburg, Germany.
*These authors contributed equally to this work.

The method described so far is capable of generating images of the spatial distribution of magnetic material. However, the mechanical movement leads to low scanning speed and the signal to noise ratio (SNR) is low owing to the weak modulation field. The mechanical movement is dispensable if three additional orthogonal homogenous magnetic fields, called drive fields, are provided (Fig. 2b). The three components of the selection field can be cancelled, at any given point in space, by appropriate adjustment of these three fields. By driving each coil pair with a predefined current waveform, the FFP can be moved on a continuous trajectory over the object. This set-up is analogous to a mechanical motion set-up.

By using drive fields, it is possible to accelerate the movement of the FFP dramatically. For this purpose, a different sinusoidal current with a high frequency is applied to each coil pair. The amplitudes of the currents must be large enough to generate magnetic fields capable of cancelling the selection field at the border of the desired region of interest. The fast FFP movement leads to a rapid local change in magnetization as soon as the FFP passes a location containing magnetic material. The magnetization change induces a signal in the recording coil that exhibits higher harmonics of the drive field frequencies. This induced signal is sufficient for image reconstruction. The modulation field with low amplitude (Fig. 1) is now obsolete. Consequently, the introduction of the drive fields overcomes both drawbacks mentioned above, namely the low encoding speed and the low SNR.

So the spatial encoding can be realized in two ways, as follows: (1) using mechanical movement, or (2) using field-induced movement of the FFP. Furthermore, both possibilities can be combined. This is the situation realized in the present experimental set-up.

The two-dimensional object used for imaging consisted of distinct holes filled with an undiluted (0.5 mol Fe^{l-1}), commercially available contrast agent (Resovist[11], Schering AG Berlin). Components used in the present set-up are illustrated in Fig. 2a. In order to form two-dimensional images, the object can be moved in two dimensions using a robot. Additionally, the drive field moves the FFP in the vertical direction. Two alternative encoding types are demonstrated. First, the robot alone is used for the spatial encoding (mechanical FFP movement). However, a drive field ($A = 10\,\mathrm{mT}\,\mu_0^{-1}$) for the generation of the harmonics is used in place of the low-amplitude modulation field, owing to the higher achievable SNR. Second, the robot provides the spatial encoding in the horizontal direction, while the drive field moves the FFP in the vertical direction. The same experiment was evaluated in both cases, but in the second case only a subset of robot scan positions was used.

Figure 3a shows an image of the object, for the case of pure mechanical movement of the object. Using a drive field leads to a contribution of neighbouring points to the recorded signal at a given robot position. This means that the simple method for generating an image (for the case of the weak modulation field) by mapping the magnitude of the harmonics is not appropriate, and a reconstruction is necessary; see Methods section.

In Fig. 3b the drive field encodes vertically and the robot is used for the horizontal encoding. As the drive field amplitude was not sufficiently high to move the FFP over the whole object, three separate images were reconstructed. They covered the upper, middle and lower regions of the object, and were averaged to form Fig. 3b. As a result, the resolution in the vertical direction is better than 0.3 mm. In the horizontal direction, the resolution is about 0.5 mm, as the derivative of the field component of the selection field in that direction is lower. The resolution in both cases (Fig. 3a and b) is the same, although the SNR differs owing to the shorter measurement time in the second case.

The theoretically expected resolution (R) is given by the ratio

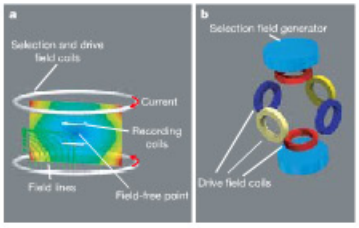

Figure 2 | The main components of the experiment, and an MPI scanner concept. **a**, The two large rings generate the selection field. Hence, a d.c. current with opposite direction in the upper and lower coil produces the sketched field (field lines and colour coded field magnitude) with the field-free point (FFP) in the centre. The same two rings serve as drive field coils, as an a.c. current is superimposed on the d.c. current. A pair of quadratic recording coils in the centre records the generated a.c. response (harmonics). **b**, The field-generating components are sketched schematically for an MPI scanner capable of encoding purely by drive fields. Two field generators produce the selection field. For each direction in space, two opposing drive field coils are used. These coils produce a more or less homogeneous field in the centre of the scanner and can therefore move the FFP.

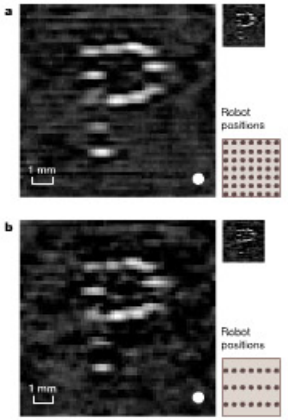

Figure 3 | Reconstructed images of the object for two different encoding types. The true size of the holes is indicated in the lower right corner of the large images. The drawings on the right side sketch the robot positions used for measurement (bottom) and a true scale image (top). In **a**, the data at all 52 × 52 robot positions were used, whereas in **b** only the data of 3 × 52 robot positions contribute to the reconstruction. In **a**, encoding is purely done by robot movement, although the FFP moves a considerable distance in the vertical direction. In **b**, this movement is exploited and the encoding is achieved partly by the drive field. The total measurement time was about 50 min, including a pure data acquisition time of 18 min for **a** and 1 min for **b**. Those spots with low intensity reflect imperfections of the object.

$2H_k/X_s$, where H_k is the a.c. field strength at which the material produces substantial higher harmonics, and X_s is the largest spatial derivative of a selection field component. A reasonable value for H_k may be obtained by equating the thermal energy with the Zeeman energy of the magnetic particles. Assuming $H_k = 0.5\,\mathrm{mT}\,\mu_0^{-1}$, reachable with particles of 30 nm diameter, and the currently used $X_s = 3.4\,\mathrm{T\,m^{-1}}\,\mu_0^{-1}$, the observed resolution is obtained.

Given that the particles have a reported diameter[11] of 4 nm it is remarkable that the achieved resolution is so high. For such particles, the Langevin theory[12] of magnetism would predict quite smooth magnetization curves with $H_k = 210\,\mathrm{mT}\,\mu_0^{-1}$, leading to a resolution of the order of 10 cm. We therefore compared the observed performance to that of ideal particle ensembles acting according to the Langevin theory. Figure 4 shows the calculated normalized signal for particles in the range 10–40 nm as a function of the number of the higher harmonics. Additionally, the observed signal and the noise level are included. The experimental data fit well, assuming that particles of 30 nm diameter are responsible for the signal. The iron mass of the signal-generating particles represents only 3% of the total iron mass.

Thus far, the reconstruction was optimized to obtain the best possible resolution. It can also be adapted to compromise resolution while improving sensitivity. Analysing the signal and noise in Fig. 4, we estimate the current detection limit to be about 100 μmol Fe^{1-} for a resolution of about 1 mm. This detection limit is already within the range of the allowed dosage for medical use[13]. However, improvements in magnetic tracers and recording electronics can be expected to lower the detection limit to 20 nmol Fe^{1-}. The potential for improvement of the tracer can be seen in Fig. 4. The signal could be increased by at least two orders of magnitude (compare red line with dashed '40 nm' line) by a better initial composition and a particle separation process. Additionally, the electronics offers significant potential for improvement. With an optimized version, we expect an improvement in SNR of between one and two orders of magnitude even for a human-size system.

The detection limit extrapolated above can be verified via comparison with magnetic resonance imaging (MRI). If the signal is induced by an oscillating magnetization M, and the object dominates the noise ('patient noise limited'), the SNR is proportional to M but independent of frequency[14]. With the detection limit of 20 nmol Fe^{1-}, the expected magnetization would still be about 5% of a typical MRI equilibrium magnetization, assuming a proton magnetization $M_{\mathrm{MRI}}(1\mathrm{T}) = 4 \times 10^{-9}\,\mathrm{T}\,\mu_0^{-1}$. So the detection limit estimated above seems to be reasonable, as the corresponding MRI signal can be detected. On the other hand, a well tolerated dosage of maghemite particles in humans[13] is about 70 μmol Fe^{1-}, resulting in an SNR two orders of magnitude higher than that achieved using MRI.

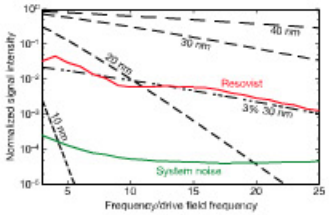

Figure 4 | Normalized signal strength as a function of frequency for simulated magnetic tracer particles and a commercially available contrast agent. The unit signal intensity is that of hypothetical maghemite particles with a step-like magnetization curve and the same iron amount as present in the commercial contrast agent, Resovist. The green line shows the measured instrumental noise of the acquisition system at a measuring time of 0.4 s. The dashed lines represent the calculated signal strength assuming a specific diameter (10–40 nm) of spherical particles acting according to the Langevin theory[12]. The total amount of iron is the same as found in Resovist. Thus, the '3% 30 nm' curve represents the expected response of an assembly of ideal particles (30 nm diameter) with an iron concentration 3% that of Resovist.

A high SNR may speed up the image acquisition, provided that an adequate encoding speed is possible. In our experiment, the coding time was rather long, but in principle coding speed can be fast in MPI. This would require the use of three orthogonal drive fields responsible for the FFP movement (Fig. 2b), as already mentioned in the basic description. In that case, the encoding time T for a volume ($N \times N \times N$ voxel) can be shown to be roughly $T = N^2/f_1$. For a drive field frequency of $f_1 = 25\,\mathrm{kHz}$ and $N = 50$, an encoding time of the order of 100 ms can be achieved. The size in each direction of a volume depends on the maximum possible shift $F = 2A/X_s$ of the FFP, which is of the order of 6 mm for $X_s = 3.4\,\mathrm{T\,m^{-1}}\,\mu_0^{-1}$ and the drive field amplitude $A = 10\,\mathrm{mT}\,\mu_0^{-1}$. For medical applications, a larger field of view as well as a higher coding speed is desired. Drive field amplitudes of up to $20\,\mathrm{mT}\,\mu_0^{-1}$, and frequencies up to 100 kHz, may be used without harming the patient through heating. To achieve a still larger field of view, an additional, slower movement of the FFP can be superimposed. Using permanent magnets, a maximum X_s of about $3\,\mathrm{T\,m^{-1}}\,\mu_0^{-1}$ seems to be possible for human applications, with reasonable effort. The potential of MPI becomes clear when considering the resolution and the encoding speed, in combination with the high SNR, which can be converted to imaging speed and/or sensitivity.

We have demonstrated the possibility of directly mapping magnetic material, without relying on the ill-posed inversion problem. This offers new opportunities for imaging magnetic tracers with high resolution and sensitivity. MPI may find a variety of applications, such as medical imaging, crack detection, polymer processing or fluid dynamics. For medical applications, such as vascular or small intestine imaging, the high resolution and sensitivity of MPI can be expected to be advantageous. Furthermore, the signal can penetrate tissues virtually unattenuated, allowing the inspection of regions located deep below the surface. Additionally, MPI does not necessarily require a large scanner. All required magnetic fields may be applied from one side. For a relatively small imaging volume, the scanner itself may be quite small and inexpensive. Finally, the method for localized interaction could be used not only for imaging, but also for therapy by local heating[15,16]. Further work will be needed to exploit the full potential of this new imaging method.

METHODS

Hardware. An outline of the MPI scanner is given in Fig. 2a. The field-producing coils of the scanner are separated by 30 mm, and do not contain ferromagnetic material. In d.c. mode, the spatial derivative of the selection field X_s at the FFP is $3.4\,\mathrm{T\,m^{-1}}\,\mu_0^{-1}$. The drive field amplitude is $10\,\mathrm{mT}\,\mu_0^{-1}$. The drive field frequency is arbitrarily set to 25.25 kHz. The two recording coils are of square shape, with about 16 mm side length and a separation of about 16 mm. They are surrounded by larger windings with opposite sense (not shown in the figure) to compensate the induced voltage due to the drive field. In addition, the recorded signal is passed through a passive notch filter. After amplification and subsequent filter stages, the signal is digitized (12 bit 20 MHz, type PCI-9812, Adlink Inc.).

A robot (Hachbettanlage 1, Isel automation KG) is used to move the sample from the upper left to the lower right corner of a square region (approximately parallel to the page plane in Fig. 2a) in subsequent horizontal lines. The resulting 52×52 data points cover a $9.4 \times 9.4\,\mathrm{mm^2}$ region.

The first test object was the letter 'P', formed by 13 holes (diameter 0.5 mm, length 1 mm) in a flat plastic plate that were filled with the magnetic tracer. In addition, a single hole (reference object) with the same dimensions was filled with tracer and used as a reference response of the entire system. Its measurement, and later use in reconstruction, accounts for all imperfections of the coils and the complex behaviour of the tracer. Both the 'P' and the reference object were measured with identical parameters (field amplitudes, frequency, robot path, delay and recording times).

Reconstruction principles. The two acquired sets of data ('P' and reference response) were both used for reconstruction. The nth harmonic $V_n(\mathbf{y})$ of the induced signal, at the robot position vector $\mathbf{y}$, can be written as:

$$V_n(\mathbf{y}) = \int G_n(\mathbf{x}+\mathbf{y})\,C(\mathbf{x})\,\mathrm{d}\mathbf{x} \qquad (1)$$

Here $C(\mathbf{x})$ is the magnetic particle concentration in the object, being unknown for the image reconstruction. $G_n(\mathbf{r})$ denotes the delta response of the system, representing the induced signal in the nth harmonic of the set-up if an infinitesimally small object is placed at position $\mathbf{r}$. This function includes all the complex dynamics of the magnetic tracer, as well as the shape of the drive field and the recording coils.

Obtaining the delta response from the reference response. Owing to the use of a relatively large object (0.5 mm diameter), it is necessary to deconvolute the delta response from the reference response before starting with the reconstruction. In order to achieve that, the spatial Fourier transform of equation (1) is used (functions in Fourier space are denoted as the corresponding lower case letters with caret):

$$\hat{v}_n(\mathbf{k}) = \hat{g}_n(\mathbf{k})\hat{c}^*(\mathbf{k}) \qquad (2)$$

After division by the known concentration function $\hat{c}^*(\mathbf{k})$ of the reference object, a Fourier back-transformation yields $G_n(\mathbf{r})$.

Matrix inversion. For image reconstruction, a direct inversion of the discretized equation (1) was used, as it gives more flexibility with respect to data reduction. The induced signal is hence:

$$V_n(\mathbf{y}_i) = \delta^2 \sum_{\mathbf{j}\in\{\mathrm{FOI}\}} G_n(\mathbf{x}_j + \mathbf{y}_i)\,C(\mathbf{x}_j) \qquad (3)$$

Here, $\mathbf{x}_j$ and $\mathbf{y}_i$ refer to different measuring positions within the scanning plane, and δ^2 is a normalization factor due to the discretization. The concentration $C(\mathbf{x})$ in equation (1) was determined numerically for each harmonic n separately, using a zero order regularization scheme[17]. This leads to several complete images of the object. Finally, the mean value over a set of these individual concentration images is computed, and shown in Fig. 3a. The grey scale was assigned to the image in a linear way. Black was assigned to the lowest obtained concentration.

Reduced data set inversion. If the robot moves only in one horizontal line, the matrix equation (1) is no longer overdetermined, and all reasonable higher harmonics have to be included in the matrix to be used for inversion. The new equation can be written as:

$$\begin{aligned} V_{n\mathrm{line}0} &= \delta^2 \textstyle\sum_{\mathbf{j}\in\{\mathrm{FOI}\}} G_{n\mathrm{line}0}(\mathbf{x}_j + \mathbf{y}_i)\,C(\mathbf{x}_j) \\ &\vdots \\ V_{n\mathrm{line}0} &= \delta^2 \textstyle\sum_{\mathbf{j}\in\{\mathrm{FOI}\}} G_{n\mathrm{line}0}(\mathbf{x}_j + \mathbf{y}_i)\,C(\mathbf{x}_j) \end{aligned} \qquad (4)$$

The inversion was performed in same way as above, but for each of the three lines independently. Finally, the three images were averaged to form Fig. 3b.

Received 10 January; accepted 12 May 2005.

1. Hevesy, G. Radioelements as tracers in physics and chemistry. *Chem. News J. Phys. Sci.* **108**, 166–167 (1913).
2. Haschek, E. & Lindenthal, O. A contribution to the practical use of photography according to Roentgen. *Wien. Klin. Wschr.* **9**, 63–64 (1896).
3. Fye, W. B. The coronary angiogram and its seminal contribution to cardiovascular medicine over five decades. *Circulation* **106**, 752–756 (2002).
4. Hendrick, R. E. & Haacke, E. M. Basic physics of MR contrast agents and maximization of image contrast. *J. Magn. Reson. Imaging* **3**, 137–148 (1993).
5. Goldberg, B. B., Liu, J. B. & Forsberg, F. Ultrasound contrast agents: a review. *Ultrasound Med. Biol.* **20**, 319–333 (1994).
6. Czernin, J. & Phelps, M. E. Positron emission tomography scanning: current and future applications. *Annu. Rev. Med.* **53**, 89–112 (2002).
7. Weissleder, R. & Ntziachristos, V. Shedding light onto live molecular targets. *Nature Med.* **9**, 123–128 (2003).
8. Heyn, C., Bowen, C. V., Rutt, B. K. & Foster, P. J. Detection threshold of single SPIO-labelled cells with FIESTA. *Magn. Reson. Med.* **53**, 312–320 (2005).
9. Nunn, A. D., Linder, K. E. & Tweedle, M. F. Can receptors be imaged with MRI agents? *Q. J. Nucl. Med.* **41**, 155–162 (1997).
10. Romanus, E. *et al.* Magnetic nanoparticle relaxation measurement as a novel tool for in vivo diagnostics. *J. Magn. Magn. Mater.* **252**, 387–389 (2002).
11. Lawaczeck, R. *et al.* Magnetic iron oxide particles coated with carbohydextran for parenteral administration and liver contrasting: Pre-clinical profile of SH U555A. *Acta Radiol.* **38**, 584–597 (1997).
12. Chikazumi, S. & Charap, S. H. *Physics of Magnetism* (Wiley, New York, 1964).
13. Weissleder, R. *et al.* Superparamagnetic iron oxide: pharmacokinetics and toxicity. *Am. J. Roentgenol.* **152**, 167–173 (1989).
14. Vlaardingerbroek, M. T. & den Boer, J. A. *Magnetic Resonance Imaging* Ch. 6.4 (Springer, Berlin, 2003).
15. Gleich, B. Method for local heating by means of magnetic particles. World patent WO2004018039 (4 March 2004).
16. Jordan, A. *et al.* Effects of magnetic fluid hyperthermia (MFH) on C3H mammary carcinoma in vivo. *Int. J. Hyperthermia* **13**, 587–605 (1997).
17. Press, W. H., Teukolsky, S. A., Vetterling, W. T. & Flannery, B. P. *Numerical Recipes in C* (Cambridge Univ. Press, 1992).

Author Information Reprints and permissions information is available at npg.nature.com/reprintsandpermissions. The authors declare no competing financial interests. Correspondence and requests for materials should be addressed to B.G. (bernhard.gleich@philips.com) or J.W. (juergen.weizenecker@philips.com).